Synergistic Interactions in Sequential Process Doping of Polymer/Single-Walled Carbon Nanotube Nanocomposites for Enhanced n-Type Thermoelectric Performance

Po-Shen Lin, Jhih-Min Lin, Shih-Huang Tung, Tomoya Higashihara,* *and Cheng-Liang Liu**

This study focuses on the fabrication of nanocomposite thermoelectric devices by blending either a naphthalene-diimide (NDI)-based conjugated polymer (NDI-T1 or NDI-T2), or an isoindigo (IID)-based conjugated polymer (IID-T2), with single-walled carbon nanotubes (SWCNTs). This is followed by sequential process doping method with the small molecule 4-(2,3-dihydro-1,3-dimethyl-1*H*-benzimidazol-2-yl)-*N,N*-dimethylbenzenamine (N-DMBI) to provide the nanocomposite with n-type thermoelectric properties. Experiments in which the concentrations of the N-DMBI dopant are varied demonstrate the successful conversion of all three polymer/SWCNT nanocomposites from p-type to n-type behavior. Comprehensive spectroscopic, microstructural, and morphological analyses of the pristine polymers and the various N-DMBI-doped polymer/SWCNT nanocomposites are performed in order to gain insights into the effects of various interactions between the polymers and SWCNTs on the doping outcomes. Among the obtained nanocomposites, the NDI-T1/SWCNT exhibits the highest n-type Seebeck coefficient and power factor of −57.7 μV K^{-1} and 240.6 μW m^{-1} K^{-2}, respectively. However, because the undoped NDI-T2/SWCNT exhibits a slightly higher p-type performance, an integral p–n thermoelectric generator is fabricated using the doped and undoped NDI-T2/SWCNT nanocomposite. This device is shown to provide an output power of 27.2 nW at a temperature difference of 20 K.

1. Introduction

Thermoelectric devices are solid-state systems that possess the unique ability to directly convert a temperature gradient into electrical energy, thereby eliminating the need for mechanical components.[1–5] This characteristic renders them highly suitable for use as the power source in wearable devices.[6–8] Extensive research has been conducted on inorganic thermoelectric materials, especially those based on chalcogenides, which have exhibited remarkable thermoelectric performance.[9–11] However, these materials are plagued by inherent brittleness and energy-intensive fabrication processes, which pose significant challenges for the production of large-area flexible thermoelectric generators (TEGs). By contrast, polymer-based and carbon-nanotube (CNT)-based thermoelectric materials offer inherent mechanical deformability,[3,12–17] thus making them promising candidates for high-performance flexible thermoelectric systems. However, the low electrical conductivities of polymer-based thermoelectric materials, along with the high thermal conductivities of their CNT-based counterparts, present obstacles to the attainment of optimal thermoelectric performance.

In recent years, significant progress has been made in enhancing the thermoelectric performance of nanocomposites composed of conjugated polymers and single-walled carbon nanotubes (SWCNTs).[18] This is because the ability to design and tailor the chemical structures of the conjugated polymers enables the effective dispersion of

P.-S. Lin, C.-L. Liu
Department of Materials Science and Engineering
National Taiwan University
Taipei 10617, Taiwan
E-mail: liucl@ntu.edu.tw

J.-M. Lin
National Synchrotron Radiation Research Center
Hsinchu 30076, Taiwan

The ORCID identification number(s) for the author(s) of this article can be found under https://doi.org/10.1002/smll.202306166

DOI: 10.1002/smll.202306166

S.-H. Tung
Institute of Polymer Science and Engineering
National Taiwan University
Taipei 10617, Taiwan

T. Higashihara
Department of Organic Materials Science
Graduate School of Organic Materials Science
Yamagata University
4-3-16 Jonan, Yonezawa, Yamagata 992-8510, Japan
E-mail: thigashihara@yz.yamagata-u.ac.jp

C.-L. Liu
Advanced Research Center for Green Materials Science and Technology
National Taiwan University
Taipei 10617, Taiwan

**ADVANCED
SCIENCE NEWS**

www.advancedsciencenews.com

NANO · MICRO

small

www.small-journal.com

the SWCNTs during the solution process, while also moderating the energy barrier between the SWCNT junctions and promoting interfacial phonon scattering.[19–21] These factors collectively contribute to an improved film quality, decreased thermal conductivity, and increased Seebeck coefficient. For instance, Jung et al. reported that the incorporation of a donor–acceptor polymer enhanced the π–π interactions between cyclopentadithiophene–pyridylthiadiazole-based copolymers and CNTs, thus leading to a denser morphology and improved electrical conductivity, along with an optimized power factor of 459 µW m^{-1} K^{-2}.[22] In previous studies, the present authors successfully fabricated polythiophene/SWCNT nanocomposites by introducing alkylthio side chain substitutes. This approach improved the dispersion of the SWCNTs via S–π and π–π interactions, thereby resulting in a high power factor of 307.7 µW m^{-1} K^{-2}.[23]

Despite the above accomplishments in developing high-performance p-type polymer/SWCNT thermoelectric devices, studies exploring n-type doping in polymer/SWCNT composites remain limited.[24,25] Pristine CNTs typically exhibit p-type thermoelectric behavior due to their susceptibility to oxygen doping during the synthesis process and storage.[26,27] However, several viable methods have been developed to transform CNTs into n-type thermoelectric materials, including ionic doping using polyelectrolyte dispersion agents or ionic liquids,[28–30] or treatment with reducing agents such as hydrazine,[31,32] calcium hydride,[33] or sodium borohydride,[34] or with amine-containing organic molecules such as polyethylenimine,[17] diethylenetriamine,[33,35] and 4-(2,3-dihydro-1,3-dimethyl-1*H*-benzimidazol-2-yl)-*N*,*N*-dimethylbenzenamine (N-DMBI).[36,37] In particular, the small molecule N-DMBI stands out due to its compatibility with both conjugated polymers and SWCNTs, which enables the simultaneous doping of the polymer and SWCNT components of the hybrid nanocomposite with N-DMBI to obtain remarkable n-type thermoelectric performance.[38–40] For example, Yin et al. demonstrated the synergistic effect between the host material and dopant in enhancing the N-DMBI doping of 4,9-dihydro-*s*-indaceno[1,2-*b*:5,6-*b′*] dithiophene-cored molecule/SWCNT composites, resulting in exceptional n-type performance with a power factor of up to 212.8 µW m^{-1} K^{-2}.[41] Liu et al. investigated the fabrication and N-DMBI doping of composite materials consisting of commercial naphthalene diimide–bithiophene copolymers (Poly{N,N'-bis(2-octyldodecyl)-naphthalene-1,4,5,8-bis(dicarboximide)-2,6-diyl]-alt-5,5'-(2,2'-bithiophene)} or P(NDI2OD-T2)) and SWCNTs at various blending ratios. The optimized n-type performance was obtained with 90 wt% SWCNTs, yielding a power factor of 27.7 µW m^{-1} K^{-2}.[42] In these studies, the observed thermoelectric performances were notably affected by the composition of each component, along with the film morphologies and microstructures. Moreover, the doping efficiency of the N-based molecule into the polymer/SWCNT nanocomposite is influenced by such factors the morphology, microstructure, and energy level differences/interactions between the components. These findings suggest that alterations in the interactions between the small molecular dopant and the polymer-wrapped CNTs can have a substantial impact on the thermoelectric performance of this ternary component system. Consequently, a more intricate doping mechanism is at play within the system, and a comprehensive understanding in this area is currently lacking.

The sequential composite fabrication and doping method has been proven to be an efficient approach for doping thermoelectric thin films.[43–47] However, as demonstrated by the above literature, a thorough understanding of the doping of N-based molecules in polymer/SWCNT nanocomposites requires an exploration of the role played by each individual component. In polymer/SWCNT nanocomposites, the SWCNTs exhibit the lower electrical resistance and are, therefore, responsible for charge transport. Meanwhile, the conjugated polymers play a crucial role in dispersing the SWCNTs, thereby ensuring their uniform distribution and intertwining among the polymer matrix to promote efficient charge transfer. In addition, the polymers act as intermediaries to minimize phonon scattering, thus leading to a reduction in the thermal conductivity and an increase in the Seebeck coefficient. Hence, in the present study, the fabrication of nanocomposites comprised of conjugated polymers and SWCNTs with exceptional n-type thermoelectric performance is achieved via sequential process doping method with the small molecular n-type dopant N-DMBI. This dopant is selected because its small size enables efficient diffusion into the nanocomposite matrix, thus resulting in improved charge transport and increased electrical conductivity. Further, various methodologies are employed herein to obtain a comprehensive understanding of the interactions among the three components and their influence on thermoelectric performance. Specifically, to investigate the diverse interactions between the polymer backbone and SWCNTs, along with their influence on the N-DMBI doping process, two naphthalene-diimide (NDI)-based conjugated polymers (NDI-T1, NDI-T2) and one isoindigo (IID)-based conjugated polymer (IID-T2) are selected. The successful fabrication of the n-type NDI-T1/SWCNT, NDI-T2/SWCNT, and IID-T2/SWCNT nanocomposites at varying doping concentrations of N-DMBI demonstrate the feasibility of the sequential composite fabrication and doping method in the polymer/SWCNT system. In addition, a comprehensive investigation of the N-DMBI/polymer, N-DMBI/SWCNT, and polymer/SWCNT interactions provides insights into the various doping mechanisms involved in the conjugated polymers and the SWCNTs. Among the N-DMBI-doped conjugated polymer/SWCNT nanocomposites, the NDI-T1/SWCNT exhibits an outstanding n-type thermoelectric performance, achieving a power factor of 240.6 µW m^{-1} K^{-2} at 323 K at a doping concentration of 0.5 mg mL^{-1}. To the best of the present authors' knowledge, this represents the highest reported value for N-DMBI-doped SWCNT composites to date. Furthermore, the fabrication of a flexible p–n integrated TEG using undoped and doped NDI-T2/SWCNT nanocomposites results in an impressive maximum power output of 27.2 nW at a temperature difference of 20 K.

2. Results and Discussion

2.1. Characterization of Polymer/SWCNT Nanocomposites

The preparation of the three selected donor–acceptor conjugated polymers (i.e., NDI-T1, NDI-T2, and IID-T2) is depicted in **Scheme 1** and detailed in the Experimental Section. Further, the results of ultraviolet photoelectron spectroscopy (UPS) and low-energy inverse photoelectron spectroscopy are provided in Figure S1 (Supporting Information). From these analyses, the highest
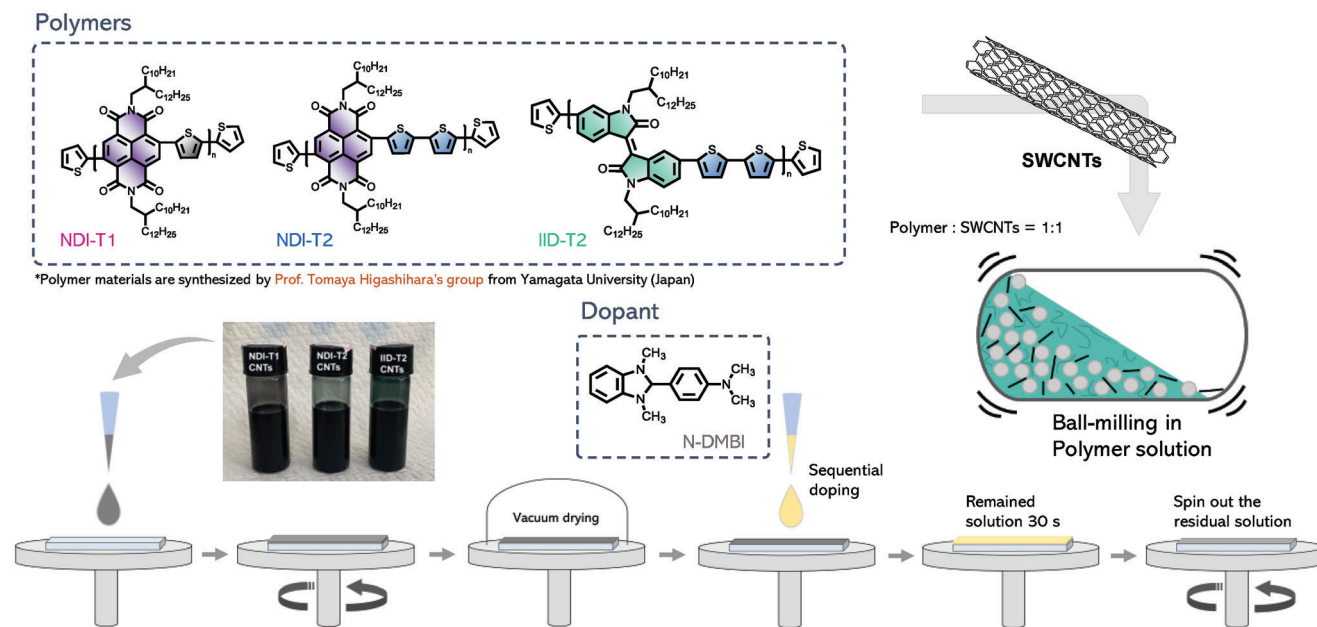
Scheme 1. The chemical structures of NDI-T1, NDI-T2, IID-T2, and N-DMBI and the fabrication process of thermoelectric thin films.

occupied molecular orbital (HOMO) levels of the NDI-T1, NDI-T2, and IID-T2 are found to be −5.90, −5.40, and −5.70 eV, respectively, and the corresponding lowest unoccupied molecular orbital (LUMO) levels are −4.10, −3.90, and −5.70 eV, respectively. In each case, the difference between the HOMO and LUMO levels has a significant impact on the energy barrier between the polymers and the SWCNT interfaces. Furthermore, the presence of different acceptors NDI or IID) and donor units (thiophene or bithiophene) within the polymer backbone leads to distinct interactions between the polymers and the SWCNTs.

The ultraviolet–visible–near infrared (UV–vis–NIR) spectra of the three polymer/SWCNT nanocomposites doped with N-DMBI concentrations of 0.1, 1.0, and 10 mg mL^{-1} are presented in **Figure 1**a–c. Here, the following three distinct absorption regions are observed: i) the region between 250 and 500 nm, which corresponds to the plasmon transition absorption of both the polymers and the SWCNTs, ii) the region between 500 and 800 nm, which is associated with the absorption of the conjugated polymer backbone, and iii) the region above 1000 nm, which corresponds to the NIR absorption of SWCNTs. A significant decrease in the absorption intensity in the second region is observed in each polymer/SWCNT nanocomposite upon the addition of the SWCNTs, thereby suggesting a modification in the original aggregation states of the pristine polymers. This is likely due to the adsorption of the polymer onto the surface of the SWCNTs. Notably, the most significant reduction in intensity in this region is observed in the IID-T2/SWCNT, thus indicating a stronger interaction between the IID-T2 polymer and the SWCNTs. This can be further elucidated from the absorption peak around 1750 in third region corresponding to the S11 transition of the SWCNTs. The suppression of S11 transition is attributed to the occupation of the conduction band by injected electrons, suggesting the successfully doping of SWCNTs.[48,49] The less suppressing of S11 transition observed in the IID-T2/SWCNTs could result by the strong interaction between polymer and SWCNTs which

prevents the injection of the electron carriers. Furthermore, an increase in the concentration of N-DMBI dopant results in a further decrease in the absorption intensity in both the second and third regions. This suggests the occurrence of electron transfer between the N-DMBI dopant and both the conjugated polymers and the SWCNTs. The explanation is supported by the magnified absorption spectra of the first region in the wavelength range of 200–500 nm in Figure S2 (Supporting Information). There, the conjugated polymers (dashed line) exhibit an absorption peak at 340–400 nm, which corresponds to the π−π* transition of the conjugated backbone.[50] Meanwhile, the undoped polymer/SWCNT nanocomposite exhibits an additional peak at 270 nm, corresponding to the π−π* transition of the C=C bonds of the SWCNTs.[51] Upon doping with increasing concentrations of N-DMBI, each polymer/SWCNT nanocomposite exhibits a slight blueshift in the π−π* transition of the SWCNTs (as indicated by the black arrow), thereby indicating the presence of interactions between the N-DMBI and the SWCNTs in all of the doped nanocomposites. Moreover, a further blueshift is observed in the π−π* electron transition of the conjugated polymers, from 396 to 350 nm for the NDI-T2/SWCNT (the blue arrow), and from 415 to 356 nm, for the IID-T2/SWCNT (the green arrow). These shifts imply that the N-DMBI interacts simultaneously with both the polymer and the SWCNTs in these two cases.[52] These results highlight the complex interactions between the different components of the polymer/SWCNT nanocomposites and the N-DMBI dopant, which can have significant implications for the thermoelectric performance of the nanocomposite.

The interaction between the polymer and the SWCNTs is further elucidated by the photoluminescence (PL) spectra of the nanocomposite solutions in the range of 570–850 nm (Figure 1d–f). When photoexcited electrons in the polymer/SWCNT nanocomposites return to the ground state, they can either emit the light or transfer their energy to the SWCNTs, thus leading to PL quenching. A higher PL quenching ratio suggests stronger
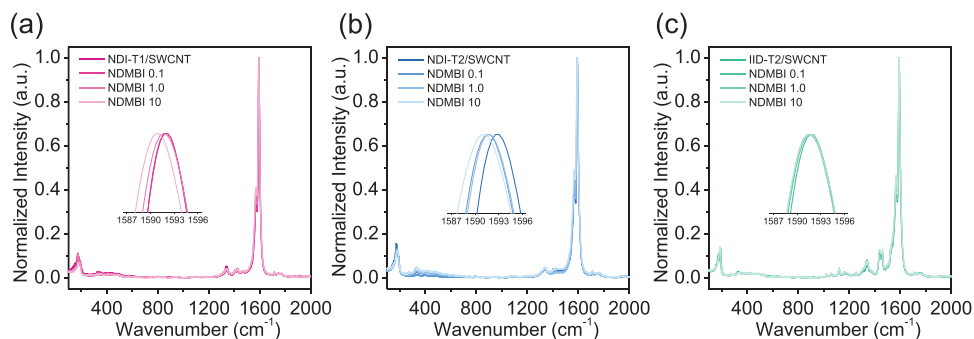
**ADVANCED
SCIENCE NEWS**
www.advancedsciencenews.com

NANO · MICRO
small
www.small-journal.com
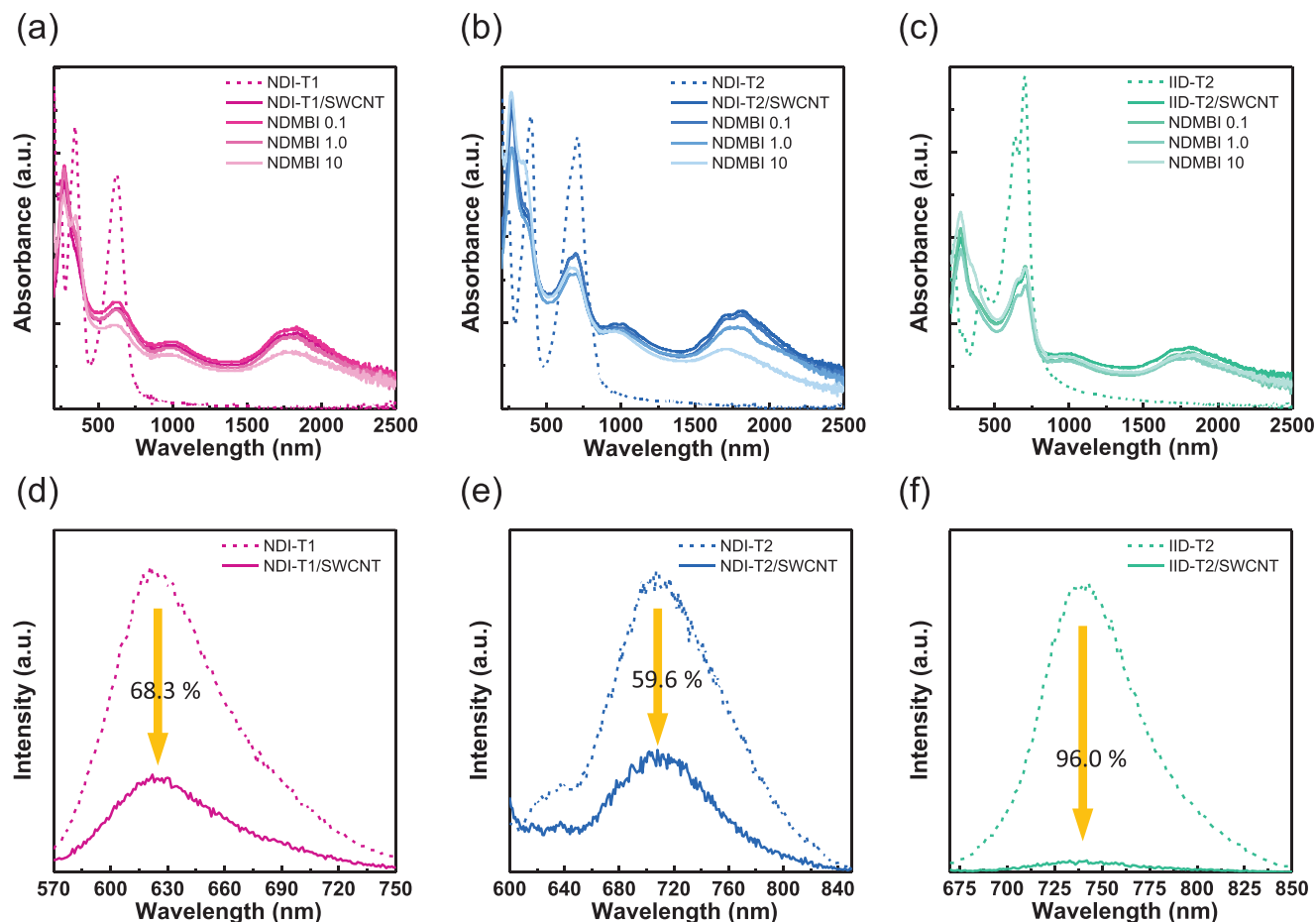
Figure 1. UV–vis–NIR absorption spectra of a) NDI-T1/SWCNT, b) NDI-T2/SWCNT, and c) IID-T2/SWCNT thin film with different N-DMBI doping concentrations. PL spectra of pristine polymers and polymer/SWCNT composites of d) NDI-T1/SWCNT, e) NDI-T2/SWCNT, and f) IID-T2/SWCNT in dilute solution.

interactions between the polymers and the SWCNTs. Thus, the results in Figure 1d–f indicate that the presence of the SWCNTs in the nanocomposite solution leads to a decrease in the PL intensity compared to that of the pristine conjugated polymer solution, thereby indicating an energy transfer from the polymer to the SWCNTs. The quenching ratios of the nanocomposite solutions were determined by calculating the ratio of the underlying area of the PL spectrum of the polymer solution with and without the addition of the SWCNTs. The results in Figure 1d–f indicate that the NDI-T1/SWCNT and NDI-T2/SWCNT nanocomposites have PL quenching ratios of 68.3% and 59.6%, respectively, while the IID-T2/SWCNT nanocomposite has a much higher PL quenching ratio of 96.0%, thus indicating the strongest interaction between the IID-T2 polymer and the SWCNTs. The result is consistent with the observations from the UV–vis–NIR absorption spectra.

The Raman spectra of the polymer/SWCNT nanocomposites with various doping concentrations are presented in **Figure 2**. There, distinct Raman shifts associated with the SWCNTs are observed, including the G band at ≈ 1590 cm^{-1} and the D band at around 1340 cm^{-1}. Moreover, only slight changes are observed in the G/D ratios before and after doping with N-DMBI, thereby indicating that the ordered structure of the SWCNTs in each

nanocomposite remains largely unaffected by doping. However, a downshift of the G band is observed in each nanocomposite, thereby indicating that the SWCNTs are also doped with the N-DMBI.[53] This downshift is more pronounced in the NDI-T1/SWCNT and NDI-T2/SWCNTs nanocomposites than in the IID-T2/SWCNT nanocomposites, which indicates that the SWCNTs in the IID-T2/SWCNT nanocomposites are less susceptible to doping with N-DMBI.

The interaction effects between the N-DMBI and SWCNTs at various doping concentrations are further elucidated by examining the radial breathing mode (RBM) region, ranging from 100 to 300 cm^{-1}, which represents the coherent movement of all carbon atoms in the radial direction (Figure S3, Supporting Information). There, the intensity of the RBM band is seen to decrease as the doping concentration of N-DMBI is increased in both the NDI-T1/SWCNT and NDI-T2/SWCNT nanocomposites (Figure S3a,b, Supporting Information), thereby indicating the effective adsorption of N-DMBI onto the surfaces of the SWCNTs.[28] In the case of the IID-T2/SWCNT, however, no consistent trend in the intensity of the RBM band with doping concentration is observed (Figure S3c, Supporting Information), thereby indicating that the interaction between the N-DMBI and SWCNTs is weaker

**ADVANCED
SCIENCE NEWS**

www.advancedsciencenews.com

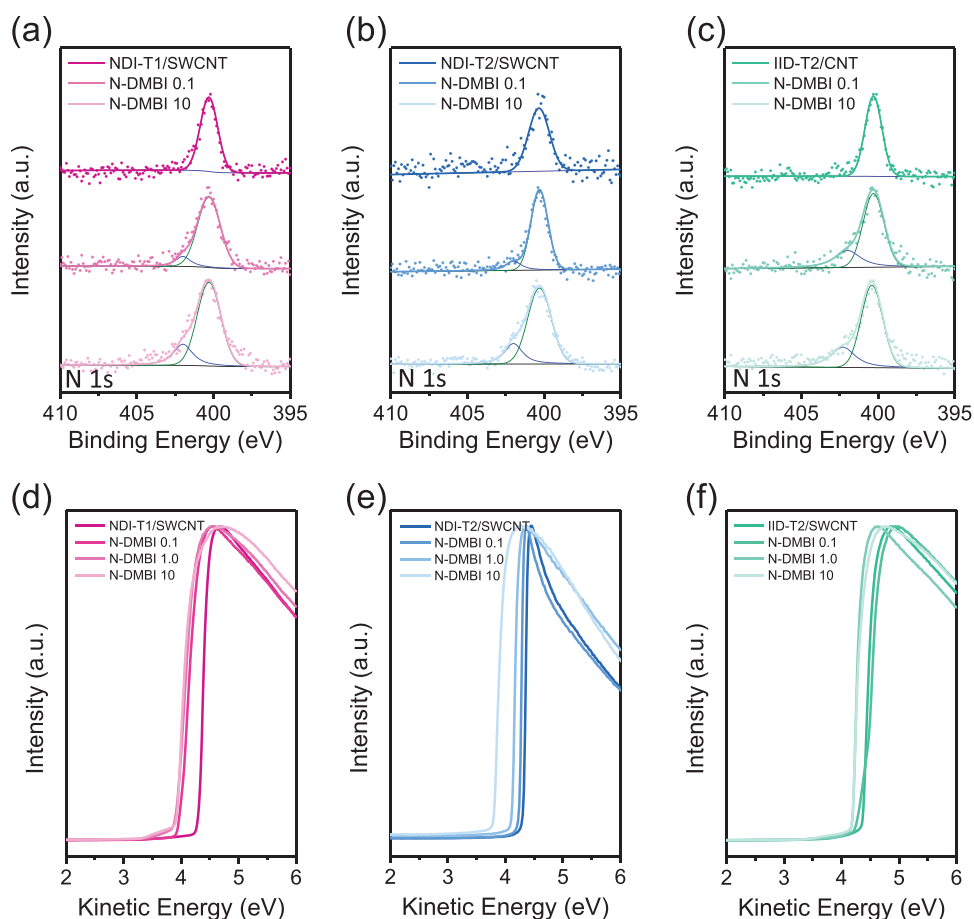**NANO · MICRO**

small

www.small-journal.com

Figure 2. Raman spectra of a) NDI-T1/SWCNT, b) NDI-T2/SWCNT, and c) IID-T2/SWCNT with different doping concentrations of N-DMBI.

than that between the IID-T2 and the SWCNTs. These results are consistent with the abovementioned PL and UV–vis–NIR spectra, which indicated strong interactions between the IID-T2 and SWCNTs. These strong interactions lead to a higher surface coverage of the SWCNTs by the IID-T2, thus leaving no available space for N-DMBI doping.

The chemical compositions of the conjugated polymer/SWCNT nanocomposites doped with various concentrations of N-DMBI are revealed by the X-ray photoelectron spectroscopy (XPS) results in **Figure 3**a–c. Here, each undoped polymer/SWCNT nanocomposite exhibits a N 1s peak at ≈400 eV due to the amide group in the main chain of the conjugated polymer. Upon doping with various concentrations of N-DMBI, however, the peak intensity and shape vary for each nanocomposite. The doping levels of the nanocomposite films can be determined by comparing this peak with that

Figure 3. XPS N 1s spectra of a) NDI-T1/SWCNT, b) NDI-T2/SWCNT, and c) IID-T2/SWCNT with different doping concentrations of N-DMBI. The normalized secondary electron cutoff of UPS spectra of d) NDI-T1/SWCNT, e) NDI-T2/SWCNT, and f) IID-T2/SWCNT with different doping concentrations of N-DMBI.

of the imidazole cation (N-DMBI$^+$) at around 402 eV. This is because the N 1s electron possesses a higher binding energy in the imidazole cation due to its oxidation state. Thus, when a low N-DMBI concentration of 0.1 mg mL^{-1} is used, the overall doping ratio in both the NDI-T1/SWCNT and NDI-T2/SWCNT nanocomposites is estimated to be ≈13:87, while that of the IID-T2/SWCNT is slightly higher at 17:83. At a higher N-DMBI doping concentration of 10 mg mL^{-1}, however, all three polymer/SWCNT nanocomposites exhibit comparable overall doping ratios of ≈35:65. It is important to clarify that this approximation indicates only the formation of N-DMBI$^+$ within each nanocomposite, whereas the individual doping ratios of the SWCNTs and the polymers remain undisclosed.

To understand the individual effects of doping upon the SWCNTs and polymers in the ternary component nanocomposite, it is essential to recognize that the SWCNTs possess significantly lower internal resistance compared to the conjugated polymers, regardless of whether they are doped or undoped. As a result, charge transfer predominantly occurs through the SWCNT network in the polymer/SWCNT nanocomposite and, hence, the work functions of the doped and undoped nanocomposites are primarily influenced by the characteristics of the SWCNTs. The changes in the work functions of the conjugated polymer/SWCNT nanocomposites upon doping with various concentrations of N-DMBI are revealed by the UPS results in Figure 3d–f. Here, the undoped nanocomposites display similar work functions of ≈4.3 eV, which are comparable to that of the pristine SWCNTs (4.3 eV, as shown in Figure S4 in the Supporting Information). Upon doping with various concentrations of N-DMBI, however, the work function is seen to gradually decrease, thereby indicating the occurrence of N doping. Thus, at a low N-DMBI concentration of 0.1 mg mL^{-1}, the work function of the NDI-T1/SWCNT exhibits a dramatic shift toward lower kinetic energy at 3.9 eV, while those of the NDI-T2/SWCNT and IID-T2/SWCNT exhibit only a slight shift to 4.2 and 4.1 eV, respectively. At higher N-DMBI concentrations of 1 and 10 mg mL^{-1}, however, the work function of the NDI-T1/SWCNT exhibits a slight shift to 3.8 eV, and that of the NDI-T2/SWCNT gradually shifts toward 3.7 eV, while that of the IID-T2/SWCNT exhibits a smaller shift to 4.1 eV. These results indicate that the SWCNTs are more easily doped with N-DMBI in the NDI-T2/SWCNT at each doping concentration, while the doping effect is limited in the IID-T2/SWCNT. These findings are consistent with the abovementioned Raman spectra.

2.2. The Morphological and Microstructural Properties of the Undoped and N-Doped Conjugated Polymer/SWCNT Nanocomposites

The microstructures of the undoped and 10 mg mL^{-1} N-DMBI-doped polymer/SWCNT nanocomposite films are revealed by the atomic force microscopy images in Figure S5 (Supporting Information). There, the undoped nanocomposite films each display intertwined networks of SWCNTs with excellent dispersion in the polymer matrix (Figure S5a–c, Supporting Information). However, the undoped NDI-T1/SWCNT exhibits a slightly larger bundle size of 30 nm (radius) compared to 20 nm each for the NDI-T2/SWCNT and IID-T2/SWCNT. Furthermore, no significant

changes in the network structures or morphologies are observed after doping with the high concentration of N-DMBI (Figure S5d–f, Supporting Information), thereby indicating that the N-DMBI molecules are uniformly distributed within the polymer/SWCNT nanocomposites without forming any small-molecule precipitates.

The grazing incidence wide angle X-ray scattering (GIWAXS) patterns of the undoped and variously N-DMBI-doped NDI-T1/SWCNT, NDI-T2/SWCNT, and IID-T2/SWCNT nanocomposite films are presented in **Figure 4**. For comparison, the GIWAXS patterns of the pristine NDI-T1, NDI-T2, and IID-T2 polymer films are also presented in Figure S6 (Supporting Information). Thus, the NDI-T1 and NDI-T2 films each exhibit face-on orientation, while the IID-T2 exhibits an edge-on orientation. Moreover, the out-of-plane region of NDI-T2 and the in-plane region of IID-T2 display distinct (010) π–π stacking peaks at $q_z = 1.65$ Å^{-1} and $q_{xy} = 1.74$ Å^{-1}, respectively. The (100) lamellar stacking distances of the pristine NDI-T1, NDI-T2, and IID-T2 polymers are found to be 26.2, 26.2, and 22.4 Å, respectively. Notably, the IID-T2 exhibits the highest crystallinity of the three polymers, with diffraction peaks up to (400) in the out-of-plane direction. This is consistent with the abovementioned PL results, where the IID-T2/SWCNT exhibits the highest PL quenching ratio due to the strong π–π interactions with the SWCNTs (Figure 1f), and with the UV–vis–NIR spectra (Figure 1c). Meanwhile, the GIWAXS patterns of the undoped polymer/SWCNT nanocomposites exhibit diffraction peaks in the range of $q = 2.0$–2.7 Å^{-1} due to the presence of the SWCNTs, and the original crystalline peaks of the pristine polymers are significantly reduced (Figure 4a–c). Moreover, the undoped NDI-T1/SWCNT nanocomposite exhibits new π–π stack peaks in the out-of-plane direction at $q_z = 1.55$ Å^{-1}, while the original π–π stack peaks of the undoped NDI-T2/SWCNT and IID-T2/SWCNT nanocomposites are similarly replaced by new and broadened π–π stack peaks in the out-of-plane direction at 1.56 and 1.59 Å^{-1}, respectively. This indicates that the addition of SWCNTs induces a rearrangement of the conjugated polymer chains, thus leading to the formation of a new microstructure embedded with the SWCNTs. After doping with N-DMBI, however, the newly formed π–π stack peaks in the out-of-plane direction are reduced for all of the polymers, and the level of reduction increases as the doping concentration is increased from 0.1 to 10 mg mL^{-1}, as shown in Figure 4d–i and Figure S7 (Supporting Information). This suggests that the N-DMBI doping influences the aggregation of the polymer chains within the nanocomposites.[54,55]

The simultaneous doping of both the conjugated polymer and the SWCNTs with N-DMBI is expected to have several effects on the thermoelectric performance of the nanocomposites. First, the facile charge transfer within the SWCNTs (referred to as intratube transfer) contributes to the increasing carrier concentration and conversion of the nanocomposite into an n-type thermoelectric material.[56,57] Second, doping the polymer component with N-DMBI extends the delocalization length of the polymer, thereby reducing the interface barrier between the SWCNTs and the polymer matrix. This, in turn, improves the charge transfer between neighboring SWCNTs via the polymer matrix (referred to as intertube transfer).[58] It is important to emphasize that the thermoelectric performance is expected to be significantly influenced by both the intratube and intertube
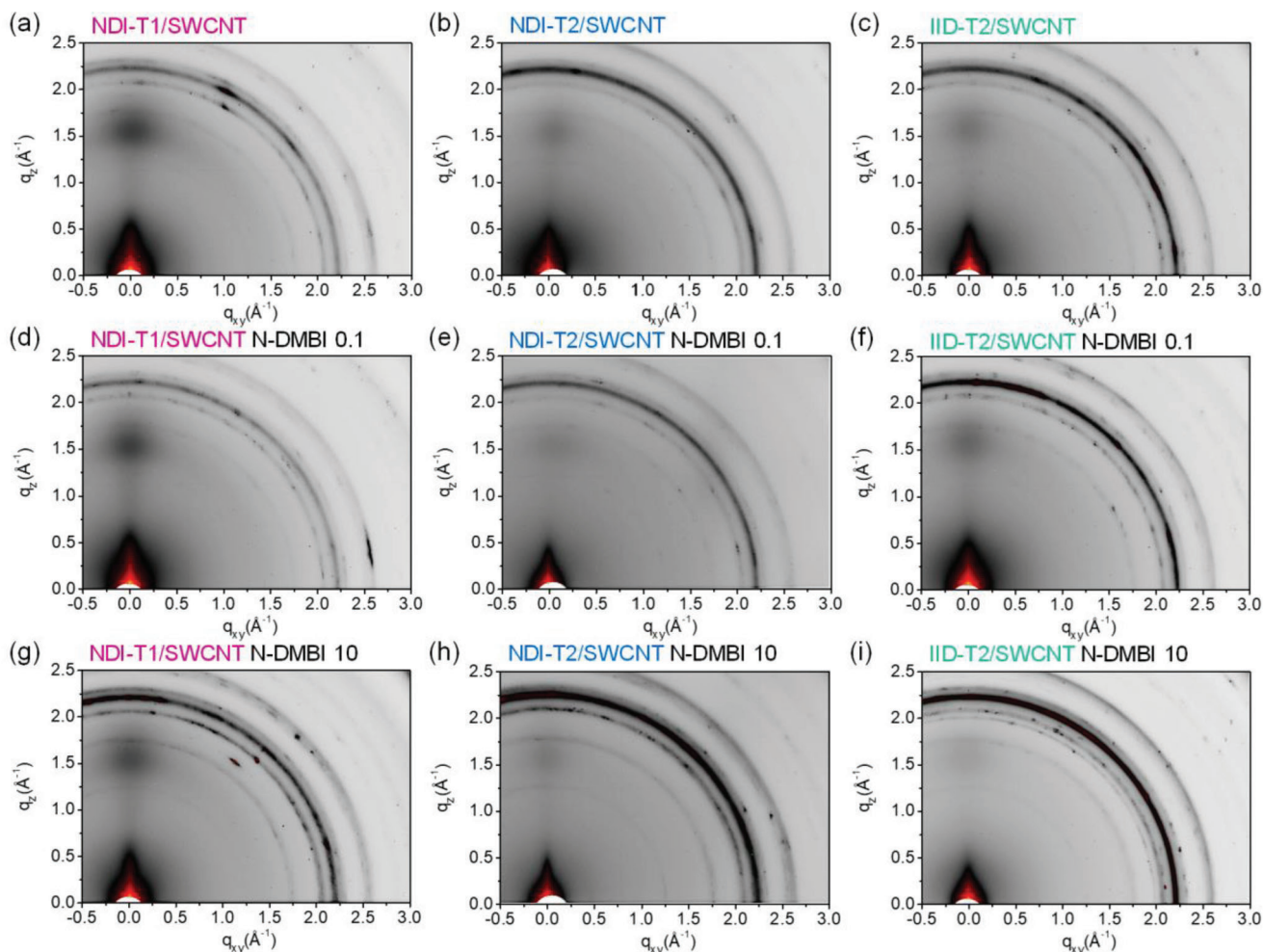
Figure 4. GIWAXS diffraction patterns of polymer/SWCNT nanocomposites with different N-DMBI doping concentrations. a–c) The pristine polymer/SWCNT nanocomposites of NDI-T1/SWCNT, NDI-T2/SWCNT, and IID-T2/SWCNT, respectively. d–f) The diffraction patterns of NDI-T1/SWCNT, NDI-T2/SWCNT, and IID-T2/SWCNT nanocomposites, respectively, with a doping concentration of 0.1 mg mL^{-1}. g–i) The diffraction patterns of NDI-T1/SWCNT, NDI-T2/SWCNT, and IID-T2/SWCNT nanocomposites, respectively, with a doping concentration of 10 mg mL^{-1}.

charge transfer processes. These processes are further examined in the following section.

2.3. Thermoelectric Properties of Doped Polymer/SWCNT Nanocomposite Thin Films

The thermoelectric properties of the undoped and variously doped conjugated polymer/SWCNT nanocomposite thin films are summarized in Tables S1–S3 (Supporting Information), and plotted in **Figure 5**a–c. Here, it is evident that the undoped NDI-T1/SWCNT, NDI-T2/SWCNT, and IID-T2/SWCNT nanocomposites each exhibit similar p-type thermoelectric behavior to that of the pristine SWCNTs, with Seebeck coefficients of 62.1 ± 2.0, 64.5 ± 2.5, and 61.7 ± 2.1 µV K^{-1}, respectively. However, distinct variations in the electrical conductivities of the undoped nanocomposites are observed, with the NDI-T2/SWCNT exhibiting a slightly higher value of up to 730.5 ± 76.6 S cm^{-1}. Moreover, the Seebeck coefficients of the nanocomposites gradually transi-

tion from positive values (p-type) to negative values (n-type) as the concentration of the N-DMBI dopant is increased. This transition occurs at a lower concentration (around 0.05–0.1 mg mL^{-1}) for the NDI-T1/SWCNT and NDI-T2/SWCNT nanocomposites than for the IID-T2/SWCNT nanocomposite, which transitions at above 0.2 mg mL^{-1}. Similarly, the NDI-T1/SWCNT and NDI-T2/SWCNT composites exhibit their maximum n-type Seebeck coefficients of −49.8 ± 6.4 and −47.3 ± 2.2 µV K^{-1}, respectively, at a N-DMBI doping concentration of 0.2 mg mL^{-1}, while the IID-T2/SWCNT exhibits its maximum Seebeck coefficient of −40.5 ± 3.2 µV K^{-1} at 0.5 mg mL^{-1} N-DMBI. Meanwhile, the electrical conductivities exhibit a consistent increase as the doping concentration is increased, with the NDI-T1/SWCNT, NDI-T2/SWCNT, and IID-T2/SWCNT each exhibiting their maximum electrical conductivities of 2180, 2741, and 1255 S cm^{-1}, respectively, at a N-DMBI concentration of 20 mg mL^{-1}. Consequently, the NDI-T1/SWCNT, NDI-T2/SWCNT, and IID-T2/SWCNT nanocomposites exhibit their maximum n-type power factors of 240.6, 230.1, and 116.4 µW m^{-1} K^{-2}, at doping concentrations of 0.5,
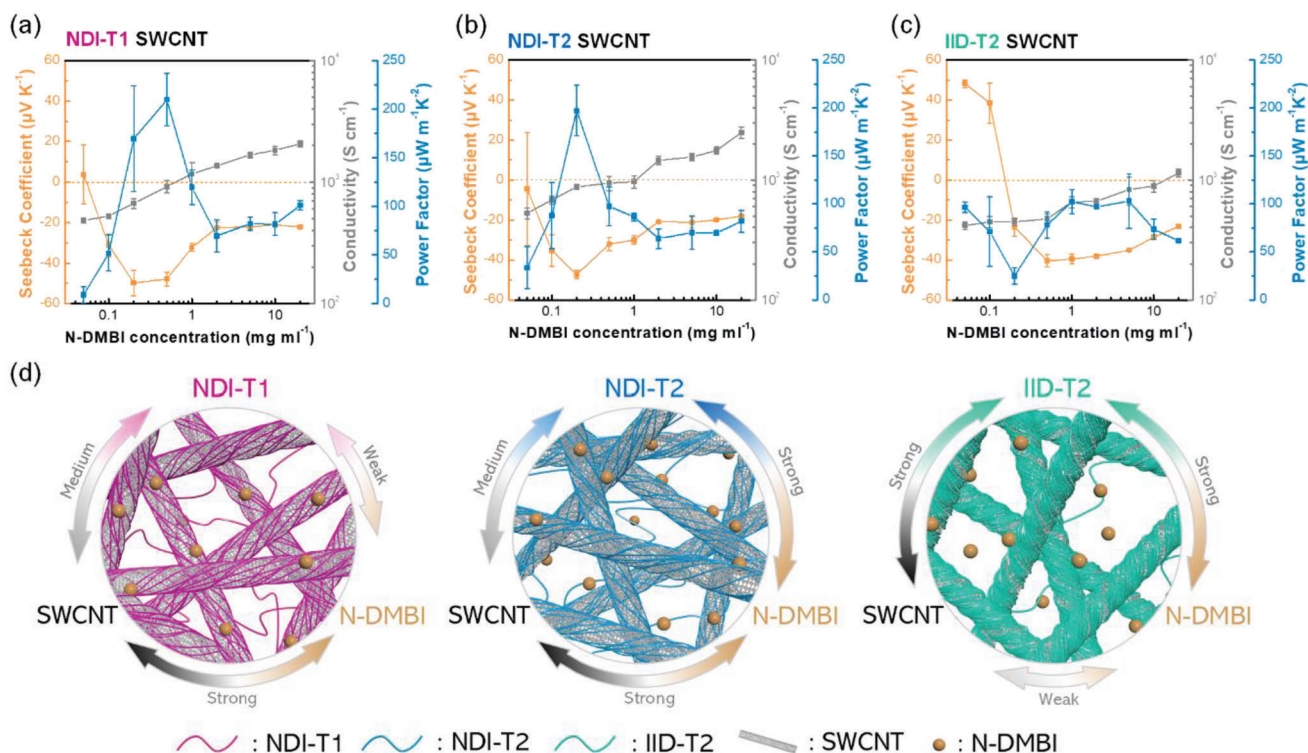
Figure 5. Seebeck coefficients, electrical conductivities, and power factors of a) NDI-T1/SWCNT, b) NDI-T2/SWCNT, and c) IID-T2/SWCNT with different N-DMBI doping concentrations. d) The proposed hypothesis regarding the N-DMBI doping mechanism of polymer/SWCNT in three-component nanocomposites.

0.2, and 1.0 mg mL^{-1}, respectively. It should be noted that increasing the doping concentrations beyond these values would gradually decrease the Seebeck coefficients while continuing to increase the electrical conductivities, because the Seebeck coefficient and electrical conductivity are interdependent.

The need for a higher N-DMBI doping concentration for the IID-T2/SWCNT to achieve n-type performance can be attributed to the pronounced interaction between the IID-T2 and the SWCNTs, as observed in the UV–vis–NIR spectra, the PL spectra, and the GIWAXS results. The high wrapping ratio of the IID-T2 on the SWCNT surface may impede the efficient doping of the latter with N-DMBI, thus resulting in a lower electrical conductivity and making the transition to n-type behavior more challenging. However, the IID-T2/SWCNT can still be doped and converted to n-type performance at a higher doping concentration, possibly due to the small size of the N-DMBI molecule, which allows it to disperse within the polymer/SWCNT nanocomposite matrix. This speculation aligns with the lower N-DMBI-doping ratio of the SWCNTs indicated by the work functions obtained from the UPS spectra at low doping concentrations of N-DMBI in the IID-T2/SWCNT. It is noteworthy that the n-type Seebeck coefficient of each polymer/SWCNT nanocomposite is associated with the concentration of N-DMBI, as the formation of N-DMBI$^+$ primarily depends on the dopant concentration. Only the IID-T2/SWCNT exhibits a slightly higher n-type Seebeck coefficient at the doping concentration above 0.5 mg mL^{-1}, which is possibly due to its higher wrapping ratio with respect to the SWCNT, thus resulting in a stronger energy filtering effect. Furthermore, the

maximum electrical conductivity of the doped polymer/SWCNT nanocomposite decreases in the order: NDI-T2/SWCNT > NDI-T1/SWCNT >> IID-T2/SWCNT. The higher electrical conductivity of the doped NDI-T2/SWCNT relative to the doped NDI-T1/SWCNT can be attributed to the stronger interaction between the NDI-T2 polymer and the N-DMBI dopant, as evidenced by the UV–vis–NIR spectra, which enables better intertube transport compared to the NDI-T1/SWCNT. Moreover, the high electrical conductivity is further facilitated by the moderate interaction between the NDI-T2 and the SWCNTs, which enables sufficient intratube transport. Consequently, the high electrical conductivity of the NDI-T2/SWCNT can be attributed to its exceptional intra- and intertube transport capabilities. It should be noted that the IID-T2 also exhibits a strong interaction with the N-DMBI. However, the inefficient doping of the SWCNTs in the IID-T2/SWCNT hampers the increase in electrical conductivity owing to poorer intratube transport in the nanocomposite.

Further insights into the N-DBMI doping mechanisms of the NDI-T1/SWCNT, NDI-T2/SWCNT, and IID-T2/SWCNT nanocomposites under high and low dopant concentrations are provided by the temperature dependence of the thermoelectric parameters in Figure S9 (Supporting Information). At the low N-DMBI concentration of 0.2 mg mL^{-1}, only a small amount of N-DMBI$^+$ is formed, and the electrical conductivity remains primarily dependent on the SWCNTs in the nanocomposite. Under this condition, both the NDI-T1/SWCNT and NDI-T2/SWCNT nanocomposites exhibit a gradual increase in electrical conductivity until reaching a peak at 450 K, followed by

a subsequent decrease (Figure S9a–c, Supporting Information). The initial increase in electrical conductivity can be attributed to semiconductor-type transport within the nanocomposite, where higher temperature leads to higher carrier mobility. The subsequent decrease in electrical conductivity above 450 K may be attributed to the loss of N-DMBI from the SWCNTs (referred to as dedoping). For the IID-T2/SWCNT, however, the electrical conductivity initially increases with temperature, then decreases at 370 K before increasing again until 510 K, followed by a subsequent decrease. Here, the lower-temperature fluctuation (310–510 K) can be attributed to a more pronounced dedoping of the IID-T2 in the nanocomposite due to the lower doping ratio of the SWCNTs, which results in a significant contribution of intertube charge transport toward the conductivity of the doped IID-T2 in IID-T2/SWCNT under these specific conditions. The second decrease in electrical conductivity at 510 K can be attributed to an additional episode of SWCNT dedoping. Notably, this additional dedoping occurs at a higher temperature than does the single dedoping of the SWCNTs in the NDI-T1/SWCNT and NDI-T2/SWCNT composites due to the stronger interaction between the IID-T2 and the SWCNTs. This stronger interaction not only hampers the doping of N-DMBI into the SWCNTs, but also impedes its subsequent dedoping. Interestingly, the latter fluctuating trend is observed in the Seebeck coefficients of all three polymer/SWCNT nanocomposites, which may further reflect the dedoping effect of the polymers in all three cases. This result suggests that the Seebeck coefficient is much more sensitive to the intertube transport at low doping concentrations, while the electrical conductivities of the doped NDI-T1/SWCNT and NDI-T2/SWCNT nanocomposites primarily depend on intratube transportation.

As shown in Figure S9d–f (Supporting Information), a high dopant concentration facilitates the sufficient doping of both the SWCNTs and the conjugated polymer matrix of the composite. Thus, when the IID-T2/SWCNT is doped with a high concentration of N-DMBI in the low temperature region, the abovementioned fluctuation in electrical conductivity disappears, and the trend becomes more similar to that of the NDI-T1/SWCNT and NDI-T2/SWCNT, albeit with a slightly higher dedoping temperature. This indicates that the trend in the electrical conductivity according to temperature depends on intratube charge-carrier transportation in all of the polymer/SWCNT nanocomposites at high doping concentrations. However, while the Seebeck coefficients of the NDI-T1/SWCNT and NDI-T2/SWCNT remain steady below 450 K, that of the IID-T2/SWCNT continuously increases, thus indicating a less stable doped state in the IID-T2/SWCNT nanocomposites. It is suggested that the dedoping process of the polymer also occurs in the NDI-T1/SWCNT and NDI-T2/SWCNT, but it is difficult to observe in the low temperature region due to the superior intratube charge transport capability of the SWCNTs in these nanocomposites.
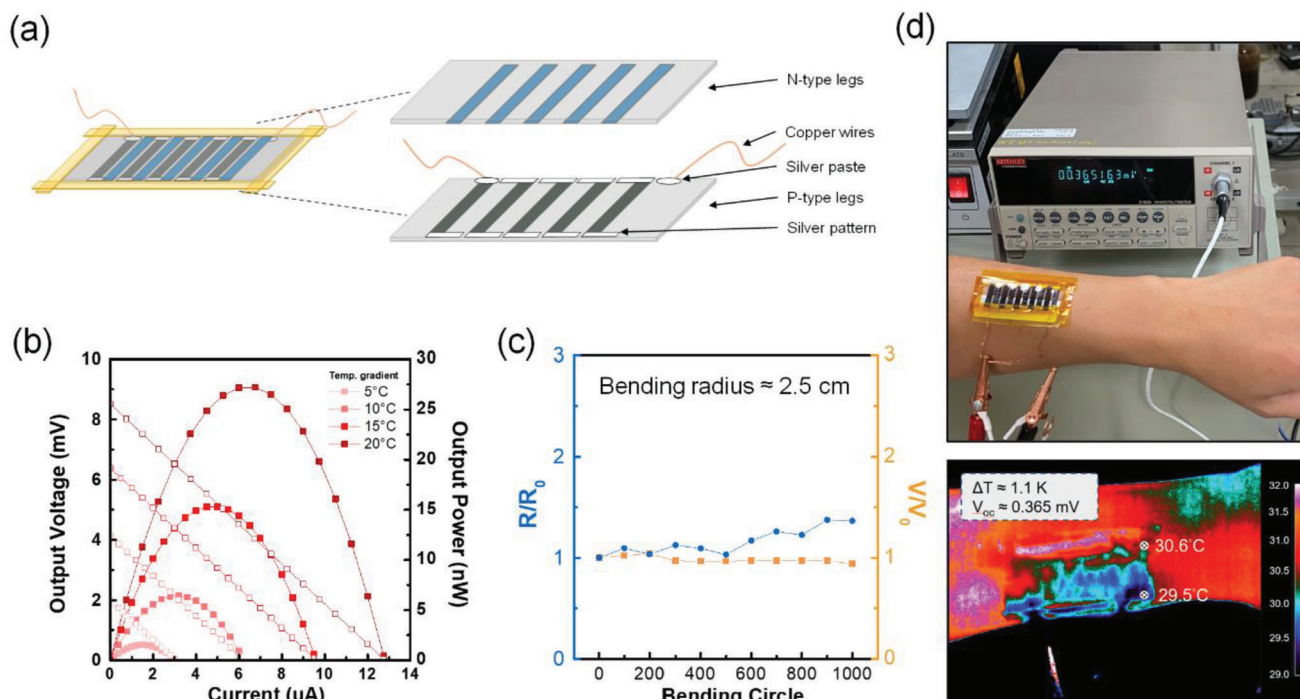
The differences between the doping mechanisms in the NDI-T1/SWCNT, NDI-T2/SWCNT, and IID-T2/SWCNT nanocomposites are shown schematically in Figure 5d. In the case of NDI-T1/SWCNT, the incorporation of the small N-DMBI molecule predominantly results in the doping of the SWCNT component with N-DMBI, thus leading to an immediate switch from p-type to n-type behavior. By contrast, the N-DMBI exhibits strong interactions with both the NDI-T2 matrix and the SWCNTs in the NDI-T2/SWCNT composite, thereby promoting improved intertube transport and contributing to a higher electrical conductivity across all doping conditions. However, the doping of the IID-T2/SWCNT composite with N-DMBI is less efficient than that of the other two nanocomposites, thereby resulting in diminished n-type thermoelectric performance. This is likely due to the strong interaction between the IID-T2 and the SWCNTs, which results in the N-DMBI being primarily doped into the IID-T2, rather than into the SWCNTs.

2.4. Evaluation of a Flexible p–n Integrated Polymer/SWCNT Composite Thermoelectric Generator

In this section, a flexible p–n integrated nanocomposite TEG is evaluated using the optimized N-DMBI-doped polymer/SWCNT nanocomposite. To ensure the achievement of a stable n-type thermoelectric performance, it is crucial to avoid utilizing low doping concentrations of N-DMBI, which are susceptible to secondary doping by oxygen in the surrounding environment.[59] As reported by Nakashima et al., the latter effect would result in a reversion to p-type performance.[60] As demonstrated in the preceding sections, the NDI-T1/SWCNT and NDI-T2/SWCNT nanocomposites exhibit similar n-type performances at high doping concentrations, while the undoped NDI-T2/SWCNT exhibits a slightly higher p-type performance. Therefore, the NDI-T2/SWCNT nanocomposite was selected for the fabrication of the flexible p–n integrated composite TEG. The configurations of the TEGs employed in this study are depicted in **Figure 6**a, and their fabrication procedure is described in the Experimental Section. The output characteristics of the flexible p–n integrated NDI-T2/SWCNT TEG under various temperature gradients (ΔT = 5, 10, 15, and 20 K) are presented in Figure 6b. Here, both the maximum current and output voltage are seen to increase as ΔT is increased from 5 to 20 K, thereby resulting in a fourfold increase in the output power. Thus, at ΔT = 20 K, the TEG achieves its maximum output voltage, current, and power of 8.02 mV, 12.75 µA, and 27.2 nW, respectively. The Seebeck coefficient (S) of the p-type leg is ≈64.5 µV K^{-1}, whereas that of the n-type leg is ≈−19.9 µV K^{-1}. Hence, the theoretical output voltage (V) obtained using the formula $V = NS\Delta T$ (where N represents the number of thermoelectric legs) is ≈8.44 mV at 20 K, which is in close agreement with the experimental value.

The notable mechanical flexibility of the NDI-T2/SWCNT nanocomposite TEG, with excellent resilience against various deformations such as bending and twisting, is indicated in Figure S10 (Supporting Information). Further, the device durability is demonstrated by its response to 1000 cycles of repeated bending to a radius of 2.5 cm and unbending in Figure 6c. Here, the device exhibits a slight increase in electrical resistance during bending, but the output voltage remains unchanged. Furthermore, the device exhibits the ability to generate electricity when in contact with the surface of human skin, as illustrated in Figure 6d. In the latter test, the successful collection of waste heat from the human skin was ensured by using foam tape to prevent direct contact between the cold side of the generator and the surface of the skin. Under these conditions, an output voltage of ≈0.37 mV was obtained at a ΔT of ≈1.1 K.

ADVANCED
SCIENCE NEWS
www.advancedsciencenews.com

NANO · MICRO
small
www.small-journal.com

Figure 6. a) Schematic representation of configuration of a p–n integrated thermoelectric generator. b) Performance characterization of output characteristic. c) Results from cyclic bending test conducted on the p–n integrated thermoelectric generator. d) Generation of output voltage resulting from the surface heat of the human body and the thermal image of the TEG.

3. Conclusions

Herein, nanocomposite thermoelectric devices were fabricated based on composites of conjugated polymers with SWCNTs. The following three conjugated polymers were investigated: NDI-T1, NDI-T2, and IID-T2. A comprehensive analysis encompassing spectroscopic examination, thin film morphological characterization, and microstructural investigation was performed to elucidate the complex mechanisms by which each nanocomposite was doped with the small molecule N-DMBI. The results revealed that the interactions between each polymer and the SWCNTs, as well as the interactions between each polymer and the N-DMBI, play crucial roles in determining the thermoelectric performance. In the case of the NDI-T1/SWCNT and NDI-T2/SWCNT, efficient doping occurs due to the appropriate wrapping ratios of the NDI-T1 and NDI-T2 polymers with the SWCNTs, which facilitates the doping of the SWCNTs with N-DMBI. Furthermore, the strong interactions within the NDI-T2/SWCNT system promote enhanced intertube charge-carrier transport, thus leading to higher electrical conductivity. However, in the case of IID-T2/SWCNT, the strong interaction between the IID-T2 and the SWCNTs hinders the efficient doping of the SWCNTs with the N-DMBI, thus resulting in a suboptimal electrical performance. Notably, the NDI-T1/SWCNT exhibited the highest n-type thermoelectric performance, with a maximum power factor of 240.6 $\mu W\ m^{-1}\ K^{-2}$. To the best of the present authors' knowledge, this represents one of the highest reported values for small-molecule-doped polymer/SWCNT nanocomposites. Furthermore, the successful realization of a p–n integrated flexible thermoelectric generator was demonstrated using the NDI-T2/SWCNT nanocom-

posite, achieving an output power of 27.2 nW at a temperature difference (ΔT) of 20 K. Additionally, the as-fabricated flexible TEG exhibited excellent mechanical properties, enduring 1000 repeated bending and unbending cycles while maintaining its thermoelectric performance. The present work contributes to a comprehensive understanding of small-molecule sequential process doping method in polymer/SWCNT nanocomposites, providing detailed insights into the doping mechanisms associated with each component. The findings presented herein are expected to serve as a foundation for future research endeavors in this field.

4. Experimental Section

Materials: The studied conjugated polymers, NDI-T1,[61] NDI-T2,[61] and IID-T2[62] were synthesized as described elsewhere. The solvents and N-DMBI small molecular dopant were supplied by Sigma-Aldrich, and used as received. Tuball SWCNTs with a purity of ≈80% were obtained from OCSiAl and employed in this study.

Preparation of the Polymer/SWCNT Nanocomposite Solution: To prepare the nanocomposite solution, NDI-based and IID-based conjugated polymers were separately dissolved in dichlorobenzene at a concentration of 1 mg mL^{-1}. Each solution was stirred at 70 °C for 1 h to ensure complete dissolution. An equal weight of SWCNTs was then added to each polymer solution, resulting in a total solid content of 2 mg mL^{-1} in each case. The resulting nanocomposite solutions were homogeneously mixed using a ball mill (Restch MM440) at 30 Hz for 20 min.

Fabrication and Measurement of the Nanocomposite Thermoelectric Devices: The as-prepared nanocomposite solution was spin-coated onto a glass substrate (15 × 15 mm^2) at a speed of 1500 rpm for 15 s. Prior to casting, the glass substrates were cleaned by successive sonication in

**ADVANCED
SCIENCE NEWS**

www.advancedsciencenews.com

**NANO · MICRO
small**

www.small-journal.com

acetone, isopropanol, and deionized water, followed by drying with N_2. The resulting nanocomposite samples were then left under vacuum for 2 min to remove any residual solvents. The thicknesses of the resulting nanocomposite films were around 30–60 nm. To fabricate each doped sample, the selected concentration (0.05, 0.1, 0.2, 0.5, 1, 2, 5, 10, or 20 mg mL^{-1}) of N-DMBI in acetonitrile was dropped onto the polymer/SWCNT nanocomposite and allowed to stand for 30 s, followed by spin coating at 3000 rpm for 20 s to remove the residual solvent. Prior to measuring the thermoelectric properties, the nanocomposite thin films were subjected to an annealing process under a nitrogen atmosphere at 190 °C for 10 min to promote better interfacial contact between the polymers and the SWCNTs. Subsequently, the nanocomposite films were cut into 7.5 × 15 mm^2 pieces, and silver paste was applied to the both ends of the device for thermoelectric measurement. The in-plane Seebeck coefficient (S) and electrical conductivity (σ) of the nanocomposite samples were measured using a commercially available thermoelectric tester ZEM-3 (Advance Riko), at an ambient temperature of 323 K under a helium atmosphere. To obtain a linear fit of the Seebeck coefficient, the temperature gradients were set at $\Delta T = 20$, 30, or 40 K. The measurements were performed with the charge transport parallel to the sample surface.

Fabrication and Measurement of the Flexible TEG: As shown schematically in Scheme S1 (Supporting Information), the flexible TEG was fabricated using the NDI-T2/SWCNT nanocomposite solution, which was doped with a high concentration of N-DMBI (10 mg mL^{-1}) to ensure the successful conversion of all the legs into n-type performance. Polyimide (PI) tape with a width of 5 mm was applied in strips onto the glass substrate, with a spacing of 3 mm. The nanocomposite solution was then bar-coated onto the glass substrate at a rate of 5 mm s^{-1}. The solvent was then removed by vacuum evaporation, and the cast/vacuum process was performed for a total 10 times to reduce the total internal resistance and obtain thermoelectric legs with a thickness of ≈500 nm. The NDI-T2/SWCNT nanocomposites were then doped with N-DMBI at a concentration of 10 mg mL^{-1} to achieve n-type behavior, while the undoped nanocomposites were used as the p-type legs. Both the n-type and p-type legs on the glass substrates were then annealed at 190 °C for 10 min. After this, a 10:1 mixture of polydimethylsiloxane (PDMS) base and curing agent was poured onto the top of the NDI-T2/SWCNT nanocomposites and cured at 80 °C for 1 h. The PDMS was then carefully peeled off from the glass substrate, resulting in transfer of the NDI-T2/SWCNT to the PDMS substrate to form a flexible thermoelectric nanocomposite film. The ends of p-type legs were patterned with thermally evaporated silver through a mask, and copper wires were attached to both ends of the device using silver paste. Finally, the n-type and p-type legs were integrated into a π-shape, and the entire TEG was sealed with PI tape.

Supporting Information

Supporting Information is available from the Wiley Online Library or from the author.

Acknowledgements

Conflict of Interest

The authors declare no conflict of interest.

Data Availability Statement

The data that support the findings of this study are available from the corresponding author upon reasonable request.

[1] T. Cao, X.-L. Shi, Z.-G. Chen, *Prog. Mater. Sci.* **2023**, *131*, 101003.
[2] S. Wang, G. Zuo, J. Kim, H. Sirringhaus, *Prog. Polym. Sci.* **2022**, *129*, 101548.
[3] Y. Zhang, W. Wang, F. Zhang, K. Dai, C. Li, Y. Fan, G. Chen, Q. Zheng, *Small* **2022**, *18*, 2104922.
[4] S. Xu, X.-L. Shi, M. Dargusch, C. Di, J. Zou, Z.-G. Chen, *Prog. Mater. Sci.* **2021**, *121*, 100840.
[5] M. Massetti, F. Jiao, A. J. Ferguson, D. Zhao, K. Wijeratne, A. Würger, J. L. Blackburn, X. Crispin, S. Fabiano, *Chem. Rev.* **2021**, *121*, 12465.
[6] Y. Jia, Q. Jiang, H. Sun, P. Liu, D. Hu, Y. Pei, W. Liu, X. Crispin, S. Fabiano, Y. Ma, Y. Cao, *Adv. Mater.* **2021**, *33*, 2102990.
[7] Y. Sargolzaeiaval, V. Padmanabhan Ramesh, T. V. Neumann, V. Misra, D. Vashaee, M. D. Dickey, M. C. Öztürk, *Appl. Energy* **2020**, *262*, 114370.
[8] A. Nozariasbmarz, F. Suarez, J. H. Dycus, M. J. Cabral, J. M. Lebeau, M. C. Öztürk, D. Vashaee, *Nano Energy* **2020**, *67*, 104265.
[9] M. Hong, M. Li, Y. Wang, X.-L. Shi, Z.-G. Chen, *Adv. Mater.* **2023**, *35*, 2208272.
[10] T.-R. Wei, P. Qiu, K. Zhao, X. Shi, L. Chen, *Adv. Mater.* **2023**, *35*, 2110236.
[11] Z.-H. Zheng, X.-L. Shi, D.-W. Ao, W.-D. Liu, M. Li, L.-Z. Kou, Y.-X. Chen, F. Li, M. Wei, G.-X. Liang, P. Fan, G. Q. Lu, Z.-G. Chen, *Nat. Sustainability* **2023**, *6*, 180.
[12] G. Prunet, F. Pawula, G. Fleury, E. Cloutet, A. J. Robinson, G. Hadziioannou, A. Pakdel, *Mater. Today Phys.* **2021**, *18*, 100402.
[13] L. Liu, J. Chen, L. Liang, L. Deng, G. Chen, *Nano Energy* **2022**, *102*, 107678.
[14] S. Masoumi, S. O'shaughnessy, A. Pakdel, *Nano Energy* **2022**, *92*, 106774.
[15] J. L. Blackburn, A. J. Ferguson, C. Cho, J. C. Grunlan, *Adv. Mater.* **2018**, *30*, 1704386.
[16] N. Komatsu, Y. Ichinose, O. S. Dewey, L. W. Taylor, M. A. Trafford, Y. Yomogida, G. Wehmeyer, M. Pasquali, K. Yanagi, J. Kono, *Nat. Commun.* **2021**, *12*, 4931.
[17] W. Zhou, Q. Fan, Q. Zhang, L. Cai, K. Li, X. Gu, F. Yang, N. Zhang, Y. Wang, H. Liu, W. Zhou, S. Xie, *Nat. Commun.* **2017**, *8*, 14886.
[18] Y. Bao, Y. Sun, F. Jiao, W. Hu, *Adv. Electron. Mater.* **2023**, *9*, 2201310.

[19] J. Liang, R. Cui, X. Zhang, K. Koumoto, C. Wan, *Adv. Funct. Mater.* **2022**, *33*, 2208813.

[20] L. Deng, Y. Liu, Y. Zhang, S. Wang, P. Gao, *Adv. Funct. Mater.* **2022**, *33*, 2210770.

[21] F. Zhang, C.-A. Di, *Chem. Mater.* **2020**, *32*, 2688.

[22] J. Jung, E. H. Suh, Y. J. Jeong, H. S. Yang, T. Lee, J. Jang, *ACS Appl. Mater. Interfaces* **2019**, *11*, 47330.

[23] P.-S. Lin, S. Inagaki, J.-H. Liu, M.-C. Chen, T. Higashihara, C.-L. Liu, *Chem. Eng. J.* **2023**, *458*, 141366.

[24] J. Tang, Y. Chen, S. R. Mccuskey, L. Chen, G. C. Bazan, Z. Liang, *Adv. Electron. Mater.* **2019**, *5*, 1800943.

[25] J. Wang, L. Liu, F. Wu, Z. Liu, Z. Fan, L. Chen, Y. Chen, *ChemSusChem* **2022**, *15*, 202102420.

[26] V. Derycke, R. Martel, J. Appenzeller, P. Avouris, *Appl. Phys. Lett.* **2002**, *80*, 2773.

[27] D. Kang, N. Park, J.-H. Ko, E. Bae, W. Park, *Nanotechnology* **2005**, *16*, 1048.

[28] S. Hata, R. Nakata, S. Yasuda, H. Ihara, Y. Du, Y. Shiraishi, N. Toshima, *Mater. Adv.* **2022**, *3*, 373.

[29] S. Yonezawa, T. Chiba, Y. Seki, M. Takashiri, *Sci. Rep.* **2021**, *11*, 5758.

[30] J. Jung, E. Hyun Suh, Y. Jeong, D.-J. Yun, S. Chan Park, J. G. Oh, J. Jang, *Chem. Eng. J.* **2022**, *438*, 135526.

[31] K. S. Mistry, B. A. Larsen, J. D. Bergeson, T. M. Barnes, G. Teeter, C. Engtrakul, J. L. Blackburn, *ACS Nano* **2011**, *5*, 3714.

[32] C. Klinke, J. Chen, A. Afzali, P. Avouris, *Nano Lett.* **2005**, *5*, 555.

[33] G. Wu, C. Gao, G. Chen, X. Wang, H. Wang, *J. Mater. Chem. A* **2016**, *4*, 14187.

[34] C. Yu, A. Murali, K. Choi, Y. Ryu, *Energy Environ. Sci.* **2012**, *5*, 9481.

[35] C. Yu, K. Choi, L. Yin, J. C. Grunlan, *ACS Nano* **2011**, *5*, 7885.

[36] Q. Hu, Z. Lu, Y. Wang, J. Wang, H. Wang, Z. Wu, G. Lu, H.-L. Zhang, C. Yu, *J. Mater. Chem. A* **2020**, *8*, 13095.

[37] N. Tanaka, T. Ishii, I. Yamaguchi, A. Hamasuna, T. Fujigaya, *J. Mater. Chem. A* **2023**, *11*, 6909.

[38] C. Dong, B. Meng, J. Liu, L. Wang, *ACS Appl. Mater. Interfaces* **2020**, *12*, 10428.

[39] K. Shi, F. Zhang, C.-A. Di, T.-W. Yan, Y. Zou, X. Zhou, D. Zhu, J.-Y. Wang, J. Pei, *J. Am. Chem. Soc.* **2015**, *137*, 6979.

[40] Y. Zeng, W. Zheng, Y. Guo, G. Han, Y. Yi, *J. Mater. Chem. A* **2020**, *8*, 8323.

[41] X. Yin, F. Zhong, Z. Chen, C. Gao, G. Xie, L. Wang, C. Yang, *Chem. Eng. J.* **2020**, *382*, 122817.

[42] Y. Liu, D. R. Villalva, A. Sharma, M. A. Haque, D. Baran, *ACS Appl. Mater. Interfaces* **2021**, *13*, 411.

[43] E. H. Suh, M.-K. Jeong, K. Lee, W. Jeong, Y. J. Jeong, I. H. Jung, J. Jang, *Adv. Funct. Mater.* **2022**, *32*, 2207886.

[44] A. Tripathi, Y. Lee, S. Lee, H. Y. Woo, *J. Mater. Chem.* **2022**, *10*, 6114.

[45] S. Deng, C. Dong, J. Liu, B. Meng, J. Hu, Y. Min, H. Tian, J. Liu, L. Wang, *Angew. Chem., Int. Ed. Engl.* **2023**, *62*, 202216049.

[46] W. Zhao, J. Ding, Y. Zou, C.-A. Di, D. Zhu, *Chem. Soc. Rev.* **2020**, *49*, 7210.

[47] T. L. D. Tam, J. Xu, *J. Mater. Chem. A* **2021**, *9*, 5149.

[48] T. Takenobu, T. Takano, M. Shiraishi, Y. Murakami, M. Ata, H. Kataura, Y. Achiba, Y. Iwasa, *Nat. Mater.* **2003**, *2*, 683.

[49] R. Shimizu, S. Matsuzaki, K. Yanagi, T. Takenobu, *Appl. Phys. Express* **2012**, *5*, 125102.

[50] Y. Yan, Y. Liu, Q. Zhang, Y. Han, *Front. Chem.* **2020**, *8*, 394.

[51] M. R. Mohammad, D. S. Ahmed, M. K. A. Mohammed, *J. Sol-Gel Sci. Technol.* **2019**, *90*, 498.

[52] Y. Zhang, S. Chen, H. Zhang, X. Ding, P. Fu, F. Du, *Compos. Commun.* **2021**, *27*, 100883.

[53] S. Qin, J. Tan, J. Qin, J. Luo, J. Jin, S. Huang, L. Wang, D. Liu, *Adv. Electron. Mater.* **2021**, *7*, 2100557.

[54] R. M. Kluge, N. Saxena, W. Chen, V. Körstgens, M. Schwartzkopf, Q. Zhong, S. V. Roth, P. Müller-Buschbaum, *Adv. Funct. Mater.* **2020**, *30*, 2003092.

[55] J. Li, C. Dong, J. Hu, J. Liu, Y. Liu, *ACS Appl. Electron. Mater.* **2021**, *3*, 3641.

[56] I. Puchades, C. C. Lawlor, C. M. Schauerman, A. R. Bucossi, J. E. Rossi, N. D. Cox, B. J. Landi, *J. Mater. Chem.* **2015**, *3*, 10256.

[57] C. Zhou, J. Kong, E. Yenilmez, H. Dai, *Science* **2000**, *290*, 1552.

[58] S. H. Kim, S. Jeong, D. Kim, C. Y. Son, K. Cho, *Adv. Electron. Mater.* **2023**, *9*, 2201293.

[59] D. Suzuki, Y. Nonoguchi, K. Shimamoto, N. Terasaki, *ACS Appl. Mater. Interfaces* **2023**, *15*, 9873.

[60] Y. Nakashima, R. Yamaguchi, F. Toshimitsu, M. Matsumoto, A. Borah, A. Staykov, M. S. Islam, S. Hayami, T. Fujigaya, *ACS Appl. Nano Mater.* **2019**, *2*, 4703.

[61] X. Guo, M. D. Watson, *Org. Lett.* **2008**, *10*, 5333.

[62] T. Lei, Y. Cao, Y. Fan, C.-J. Liu, S.-C. Yuan, J. Pei, *J. Am. Chem. Soc.* **2011**, *133*, 6099.

2306166 (12 of 12)